



## Experimental and DFT studies of $Pb^{2+}$ adsorption on the surface of magnetic nanoparticles modified polythiophene

Mohammad Soleimani Lashkenari<sup>a</sup>, Fateme Entezari Juybari<sup>b</sup>, Arash Kamran-Pirzaman<sup>c</sup>, Leila Tabari<sup>d</sup>, Mohsen Ghorbani<sup>e,\*</sup>

<sup>a</sup>Fuel Cell Electrochemistry and Advanced Material Research Laboratory, Faculty of Engineering Modern Technologies, Amol University of Special Modern Technologies, Amol, 4616849767, Iran, email: m.soleimani@ausmt.ac.ir (M.S. Lashkenari)

<sup>b</sup>University of Science & Technology of Mazandaran, Chemical Engineering Department, Behshahr, Iran, email: hoda\_entezari@yahoo.com (F.E. Juybari)

<sup>c</sup>Faculty of Chemical Engineering, University of Science & Technology of Mazandaran, P.O. Box 48518-78413, Behshahr, Iran, Tel. ++98-11-33552022,23, Fax ++98-11-34552022, email: A.kamran@mazust.ac.ir (A. Kamran-Pirzaman)

<sup>d</sup>Department of Physical Chemistry, Faculty of Chemistry, University of Mazandaran, P.O. Box 453, Iran, email: tabari1384@yahoo.com (L. Tabari)

<sup>e</sup>Department of Chemical Engineering, Babol Noshirvani University of Technology, Shariati Ave., Babol, Iran, Post Code: 47148-71167, Fax +981133234201 email: m.ghorbani@nit.ac.ir (M. Ghorbani)

Received 13 August 2018; Accepted 17 February 2019

### ABSTRACT

In this study, a new effective  $Pb^{2+}$  ions adsorbent is obtained by surface modification of magnetic ( $Fe_3O_4$ ) nanoparticles with polythiophene (PTh). The morphology and structure of  $Fe_3O_4$ /PTh nano-adsorbents are determined by scanning electron microscopy (SEM) and transmission electron microscopy (TEM). Formation of  $Fe_3O_4$ /PTh nanocomposite is confirmed by Fourier transform infrared spectroscopy (FTIR) analysis. Then the effective factors on process adsorption were investigated including pH of the solution, the initial concentration of  $Pb^{2+}$  ions in the solution, adsorbent dosage, temperature and the contact time. According to the findings, the maximum adsorption capacity is achieved at pH 6, temperature 60°C and 10 g/L adsorbent dosage. The Sips and pseudo-second-order equation have been shown maximum acceptable correlation coefficient ( $R^2$ ) among the adsorption and kinetic equations. Sips isotherm capacity in terms of monolayer adsorption is obtained 47.577 mg/g. From DFT calculations, it is found that  $Pb^{2+}$  ion adsorbs with the significant adsorption energy, but has negligible effects on the electronic structure of  $Fe_3O_4$ /PTh nanocomposite. The values of enthalpy ( $\Delta H^\circ$ ) and Gibbs free energy ( $\Delta G^\circ$ ) are positive and negative, respectively, confirming the endothermic and spontaneous nature of adsorption. Also, desorption studies represent acceptable results in 5 cycles.

**Keywords:** Magnetite; Polythiophene; Heavy metals; Density functional theory

### 1. Introduction

Water contamination by heavy metal ions such as nickel ( $Ni^{2+}$ ), cadmium ( $Cd^{2+}$ ), and lead ( $Pb^{2+}$ ) has become a serious environmental issue because of their destructive impact on both nature and well-being. Heavy metals are

non-biodegradable and likewise can accumulate along the food chain. These metals find their ways to the environment mainly through different industrial activities such as glass, battery, metallurgical alloying, mining, ammunition, printing, and ceramics.  $Pb^{2+}$  is an extremely toxic substance and has dangerous health effect on all ages. The World Health Organization (WHO) recommended the maximum acceptable  $Pb^{2+}$  concentration of 0.01 mg/L in drinking

\*Corresponding author.

water and IS 10500 1992 identified the maximum  $\text{Pb}^{2+}$  concentration of 0.10 mg/L for discharge into inland surface water [1]. Accordingly, the removal  $\text{Pb}^{2+}$  ion in wastewater is essential prior to discharging it into the environment by a reliable method. Several separation methods are available such as chemical precipitation, coagulation, ion-exchange, flocculation, reverse osmosis and adsorption process. Adsorption is one of these methods that has been known as the most effective low-cost alternatives process in use for the removal of contaminants from water. Efficient adsorbent have a key impact on the removal of heavy metal from the water solution by adsorption process. The poor adsorption capacity of common adsorbents causes growing demand to discover relatively efficient, low cost and easily available adsorbents. Great interests have arisen in the application of activated carbon as sorbent because of the positive results yielded from removing the heavy-metal ions [2], but the use of this adsorbent is not economically reasonable [3]. The use of nanoparticles for heavy metal removal from water/wastewater has been one of the trending topics in the recent literature. The unique features of nano-sorbents have led to advantageous results over the traditional adsorbents and they have presented efficient and reasonable ways to the removal of metal. Different types of nanoparticles were used for the same goal and they demonstrated good adsorption efficiency. The large surface areas and short diffusion length in nanoparticles which lead to high adsorption capacity [4] and also more multiple sites for interaction or adsorption with metallic species result in improving adsorption process. Nevertheless, one of the main problems of using nano-sorbents for removing heavy metal ions from water/wastewater is the separation and filtration of them from the solution for their small size and dispersion in the medium [5]. Over the years, many scientists have focused their attentions on magnetizing adsorbents and use magnetic separation to overcome these limitations [6]. Magnetic nanoparticles can be separated from the aqueous solution through using an external magnetic field and they have been demonstrated as an easy and economical method for sorbent recovery. In recent years, the nano-sized particles have attracted attentions because of the wide applications in enzyme immobilization [7], DNA extraction [8], drug delivery [9], immunoassay [10], environmental remediation [11], catalysis [12], and sensors [13]. The iron oxides had gained so much research interest for their chemical stability, nontoxicity, and low cost. One of the most common iron oxides is magnetite which contains both  $\text{Fe}^{2+}$  and  $\text{Fe}^{3+}$  and has an inverse spinel crystal structure [14]. Recently, a lot of researches have been focused on utilization of magnetite in wastewater treatment. According to Xue et al. [15], nanoscale magnetite has shown considerable potential as an adsorbent to remove  $\text{Cu}(\text{II})$  from aqueous solutions. It was reported that magnetite nano-rods have been used for the removal of different heavy metals from aqueous solution. However, this adsorbent suffers from easy aggregation and uncontrolled oxidation. Taking a suitable coating is a possible solution to this problem. The magnetite coated materials for heavy metal removal have widely been employed for the improvement of treatment capacity, in contrast with uncoated adsorbents, such as polypyrrole [4], polyrhodanine [16] and chitosan [17].

Conductive polymers have been the target of many studies in different fields such as, rechargeable battery [18], electromagnetic interference (EMI) shielding [19], chemical sensor [20], photovoltaic cell [21], gas separation membranes [22], enzyme immobilization matrices [23], corrosion devices [24], water and wastewater treatment [25] and microwave absorption [26]. Among numerous conducting polymers, polythiophene (PTh) is a common conducting polymer and has attracted much attention because of the great number of functionalities such as chemical stability, high conductivity, convenience in preparation and also molecular chain structure adjustability. These features make PTh a good choice as a surface modifier that combines magnetic cores with PTh shells.

Herein, iron oxide ( $\text{Fe}_3\text{O}_4$ ) nanoparticles were successfully encapsulated by PTh to obtain an efficient sorbent which can be magnetically separated and has a high capacity for  $\text{Pb}(\text{II})$  ions removal. Characteristic of prepared nanocomposite demonstrated the presence of magnetite and PTh in samples. Furthermore, the effects of temperature, initial pH, contact time, adsorbent dosage and initial  $\text{Pb}(\text{II})$  concentration on the  $\text{Pb}(\text{II})$  removal efficiency were assessed.  $\text{Pb}(\text{II})$  removal properties were investigated through adsorption isotherms and kinetics and desorption studies were conducted. Finally, DFT calculations were utilized to find the adsorption energy of  $\text{Pb}^{2+}$  ion with the  $\text{Fe}_3\text{O}_4/\text{PTh}$  nanocomposite.

## 2. Materials and methods

### 2.1. Chemicals

Merck chemical products have been bought for the current study including  $\text{FeCl}_3 \cdot 6\text{H}_2\text{O}$ ,  $\text{FeSO}_4 \cdot 7\text{H}_2\text{O}$ , ammonia solution (25 wt. %), ethanol, thiophene, acetonitrile, hydrogen peroxide ( $\text{H}_2\text{O}_2$ ) for preparation of nano sorbent and hydrochloric acid, sodium pills, lead nitrate ( $\text{Pb}(\text{NO}_3)_2$ ) for  $\text{Pb}(\text{II})$  removal, and they were used without further purification except for the thiophene monomers.

### 2.2. Preparation of nano sorbent

The co-precipitation method was applied to synthesis  $\text{Fe}_3\text{O}_4$  nanoparticles and then they were coated by chemical oxidative polymerization of thiophenes monomers, using a similar method reported in our previous work [27]. Briefly, an aqueous solution including  $\text{FeCl}_3 \cdot 6\text{H}_2\text{O}$  and  $\text{FeSO}_4 \cdot 7\text{H}_2\text{O}$  in deionized water was heated to 80°C and then a 200 ml of 2 M ammonium solution was added to the mentioned solution. The produced precipitation was collected by magnetic separation and after washing with distilled water and ethanol was dried in vacuum at 50°C for 24 h. In the next stage, 0.5 g of dried sample was dispersed in acetonitrile solution by sonication and afterward thiophene monomers were added to the solution. After that, thiophene monomers were polymerized on magnetite nanoparticles by  $\text{FeCl}_3$  as an oxidant. After dropping 5 ml of  $\text{H}_2\text{O}_2$ , the mixture was stirred for 5 h in surround temperature. As noted in above, made precipitation was attracted using a magnet, washed with distilled water and ethanol several times and oven dried at 50°C for 20 h.

### 2.3. Instrumentation

The morphology of the magnetite and Fe<sub>3</sub>O<sub>4</sub>/PTh samples were analyzed by a Field Emission Scanning Electron Microscope (EM3200, KYKY). A Transmission Electron Microscope (TEM, Zeiss - EM10C, 120 keV) was used to determine the exact physical properties of particles. The presence of functional groups on the nanocomposite was measured by examining the samples via the Fourier Transform Infrared Spectrometry (FTIR, BRUKER, Model tensor 27) by pressing powder into a pellet and using KBr as a matrix in the wavenumbers of 4000–400 cm<sup>-1</sup>. The identification of the presence of the element in the samples, both before and after adsorption, was performed by Energy-Dispersive X-Ray Spectrometer (EDX, sirios SD). The Pb(II) concentration before and after the adsorptive reaction was obtained through an Inductively Coupled Plasma Spectrometer (ICPS-7000).

### 2.4. Batch experimental systems

#### 2.4.1. Adsorption studies

Experimental adsorption studies were done at ambient temperature by agitating 10 g L<sup>-1</sup> of the Fe<sub>3</sub>O<sub>4</sub>/PTh nano-composite in 50 mg L<sup>-1</sup> of Pb(II) solution in a thermostatic shaker rotated at 300 rpm for 2 h.

To maintain magnetic properties and avoiding the precipitation of Pb(OH)<sub>2</sub>, pH was investigated from 2 to 6 and was adjusted with hydrochloric acid and sodium hydroxide solution. The effect of adsorbent dose, contact time and temperature was studied at Pb(II) concentration of 50 mg L<sup>-1</sup> at the optimum pH. After each adsorption test, the adsorbent was separated from the liquid magnetically and the final concentration of the lead ions in the aqueous sample was calculated via inductively coupled plasma (ICP) analysis. The isotherm, kinetic and thermodynamic studies were constructed by the data obtained at different initial concentrations, contact times and temperature, respectively. The removal efficiency of metal ion onto the Fe<sub>3</sub>O<sub>4</sub>/PTh nano-sorbent was calculated by the equation below:

$$\% \text{ Removal Efficiency} = \frac{C_0 - C_e}{C_0} \times 100 \quad (1)$$

where  $C_0$  and  $C_e$  stand for the initial and the equilibrium Pb(II) concentration, respectively, in mg L<sup>-1</sup>. The amount of sorption capacity at the time  $t$ ,  $q_t$  (mg/g), was obtained as follows:

$$q_t = \frac{C_0 - C_t}{M} V \quad (2)$$

where  $C_0$  and  $C_t$  (mg L<sup>-1</sup>) were the liquid-phase concentrations of solutes at initial and a given time  $t$ ,  $V$  is the volume of the solution in liter and  $M$ , the mass of Fe<sub>3</sub>O<sub>4</sub>/PTh nano-sorbent in gram. The amount of adsorption at equilibrium,  $q_e$ , was defined by the following formula:

$$q_e = \frac{C_0 - C_e}{M} V \quad (3)$$

In that  $C_e$  (mg L<sup>-1</sup>) was the Pb(II) ion concentration at equilibrium.

#### 2.4.2. Desorption studies

The desorption experiments were conducted at ambient temperature blending 10 g L<sup>-1</sup> of the adsorbent with 50 mg L<sup>-1</sup> metal ions solution and pH of 6 in a batch mode. In order to achieve the desorption of Pb(II) from Pb-loaded Fe<sub>3</sub>O<sub>4</sub>/PTh nano-adsorbents, 0.1 M HCl solution was used. Then Fe<sub>3</sub>O<sub>4</sub>/PTh nano-adsorbents were purified for a couple of times using distilled water so that the outcome would be free of excess acid. Finally, the adsorbent was dried and reused in the adsorption process. The reusability of the adsorbent was evaluated by repeating the described adsorption-desorption cycle for five times consecutively using the same adsorbent.

### 2.5. Computational details

DMol3 program in Materials Studio was utilized for obtaining the Density functional theory (DFT) calculation [28]. Accordingly, the spin-unrestricted generalized gradient approximation (GGA) with the Perdew–Burke–Ernzerhof (PBE) functional was used to introduce the total electronic energy of exchange-correlation [29]. A real-space cutoff of 5.00 Å and the double numerical plus polarization function basis sets (DNP) with no symmetry constraints were employed to improve the computational performance [30]. Recently, The DNP and GGA/PBE functional results are widely used to study the adsorption characteristics of molecules on the adsorbent surface [31]. The adsorption energy ( $E_{ad}$ ) of Pb(II) on the surface of the Fe<sub>3</sub>O<sub>4</sub>/PTh nano-composite is stated as follows:

$$E_{ad} = E_{tot}(Fe_3O_4 / Polythiophene + Pb(II)) - [E_{tot}(Fe_3O_4 / Polythiophene) + E_{tot}(Pb(II))] \quad (4)$$

where  $E_{tot}(Fe_3O_4 / Polythiophene + Pb(II))$  is the total energy of the adsorption structure of Pb on the surface of Fe<sub>3</sub>O<sub>4</sub>/PTh nano-adsorbent;  $E_{tot}(Pb)$  is the total energy of the Pb(II) and  $E_{tot}(Fe_3O_4 / PTh)$  is the total energy of the Fe<sub>3</sub>O<sub>4</sub>/PTh nano-composite. The negative and positive values of  $E_{ad}$  indicates the exothermic and endothermic processes, respectively.

## 3. Results and discussion

### 3.1. Experimental and theoretical characterization of Fe<sub>3</sub>O<sub>4</sub>/PTh

To identify functional groups in the synthesized sample and confirm the formation of the Fe<sub>3</sub>O<sub>4</sub>/PTh nanocomposite, FTIR analyses were done and are indicated in Fig. 1. The peak around 590 cm<sup>-1</sup> corresponds to the vibration of the Fe-O bonds and indicates the presence of magnetite in the sample. Other additional peaks in the curve are related to PTh coating. The peak at 672 cm<sup>-1</sup> can be attributed to the stretching of the C-S in the thiophene ring. Two peaks at 796 and 1084 cm<sup>-1</sup> denote the C-H out-of-plane deformation mode and C-H in-plane deformation mode, respectively. The observed peak at 1225 cm<sup>-1</sup> belongs to C-C stretching vibration and indicates thiophene was synthesized in sample correctly. The peak at 1681 cm<sup>-1</sup> is assigned stretching vibration of C=C that covered characteristic peak of related

magnetite  $\text{Fe}_3\text{O}_4$ . The peak at  $2362\text{ cm}^{-1}$  is attributed to gaseous  $\text{CO}_2$  in spectrometer's chamber. Wide band in the area of  $3400\text{ cm}^{-1}$  can be attributed to O-H stretch.

The morphology of synthesized nano-adsorbent was studied by using scanning electron microscope (SEM) and transmission electron microscopy (TEM). Fig. 2a shows the SEM image of  $\text{Fe}_3\text{O}_4/\text{PTh}$  revealing small particles, spherical and uniform in distribution. TEM image in Fig. 2b shows well-defined particles which confirm the  $\text{Fe}_3\text{O}_4$  nanoparticles are surrounded by PTh. The bright and dark spots in the sample can be attributed to PTh shell and magnetite core, respectively. Through TEM observation it can be confirmed that the average size of the core and shell is 15 and 5 nm, respectively.

In theoretical section, at first, the optimized molecular structures of the  $\text{Fe}_3\text{O}_4$  and PTh have been calculated using DFT. Then, we performed full structural optimization of the  $\text{Fe}_3\text{O}_4$  molecule on the surface of the segment of PTh molecule, without any symmetry constraints, to find the most stable structure of the  $\text{Fe}_3\text{O}_4/\text{PTh}$  nanocomposite.

The obtained values from optimized geometries of PTh show that average lengths of the C–C and S–C bonds are  $1.407\text{ \AA}$  and  $1.755\text{ \AA}$ , respectively. The calculated bond

angles are found to be about  $113.32^\circ$  for C–C–C of pentagonal rings of PTh and  $92.17^\circ$  for C–S–C angles. All of the findings are in good accordance with the previous experimental and theoretical studies [32,33]. After locating magnetite on PTh molecule the small changes are found in the bond lengths and bond angles. Fig. 3 shows the most stable configuration of the  $\text{Fe}_3\text{O}_4/\text{PTh}$  nanostructure.

The impact of magnetite on the electronic properties of the PTh was examined by the HOMO (highest occupied molecular orbital) and LUMO (lowest unoccupied molecular orbital) energy surfaces and transferred Mulliken charge is calculated. Table 1 shows the calculated HOMO and LUMO energies, energy gap ( $E_{\text{LUMO}} - E_{\text{HOMO}}$ ), formation energy ( $E_f$ ) of  $\text{Fe}_3\text{O}_4/\text{PTh}$  structure and the Mulliken charge of magnetite molecule.

As shown in Table 1, energy gap of  $\text{Fe}_3\text{O}_4/\text{PTh}$  is smaller than PTh which leads to easier electron transport through  $\text{Fe}_3\text{O}_4/\text{PTh}$  nanocomposite. A small energy gap shows that adding electrons to LUMO or removing electrons from a

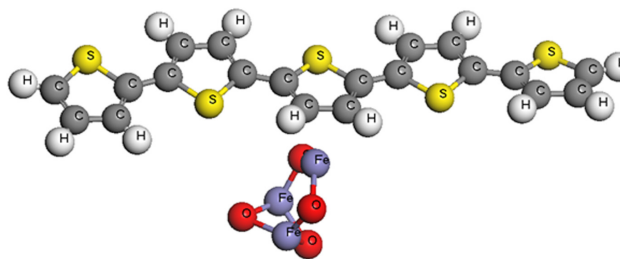


Fig. 3. The optimized most stable configuration of  $\text{Fe}_3\text{O}_4/\text{PTh}$ .

Table 1  
Calculated energies of HOMO and LUMO, energy gaps, formation energy ( $E_f$ ) of  $\text{Fe}_3\text{O}_4/\text{PTh}$  structure and the Mulliken charge of  $\text{Fe}_3\text{O}_4$ . (All energies are in eV)

	$E_{\text{HOMO}}$	$E_{\text{LUMO}}$	Energy gap	$E_f$	Mulliken charge of $\text{Fe}_3\text{O}_4$ (e)
PTh	-4.49	-2.84	1.65	-	-
$\text{Fe}_3\text{O}_4/\text{PTh}$	-4.20	-3.70	0.50	-0.92	-0.1

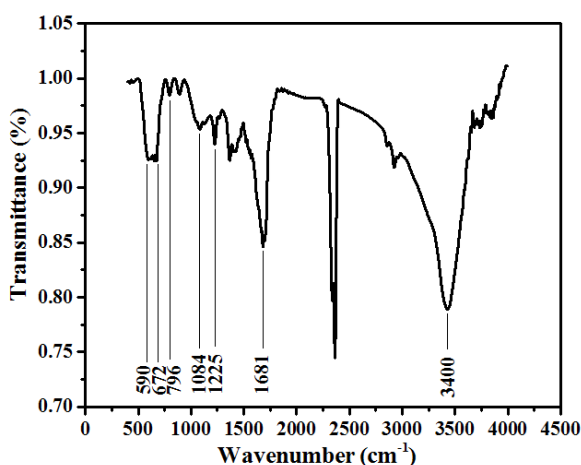


Fig. 1. FTIR spectra of the  $\text{Fe}_3\text{O}_4/\text{PTh}$  nanocomposite.

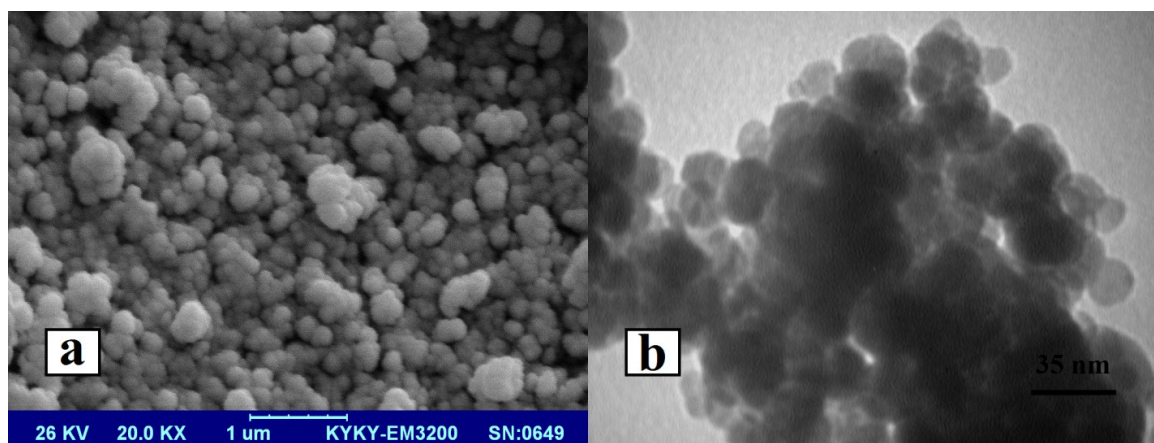


Fig. 2. SEM (a) and TEM (b) images of the  $\text{Fe}_3\text{O}_4/\text{PTh}$  nanocomposite.

HOMO is desirable with regard to the energy. Therefore,  $\text{Fe}_3\text{O}_4/\text{PTh}$  nanocomposite has a better electronic structure for adsorption than the pristine PTh.

As seen in Table 1 the calculated formation energy ( $E_{\text{Fe}_3\text{O}_4/\text{PTh}} - E_{\text{Fe}_3\text{O}_4} + E_{\text{PTh}}$ ) is  $-0.92\text{eV}$  ( $-89.12\text{kJ/mol}$ ). The negative formation energy indicates the thermodynamic stability of composite. The obtained result of Mulliken charge value shows that the charge of  $0.1e$  transfers from the PTh to the  $\text{Fe}_3\text{O}_4$  molecule.

To derive information about the charge distribution the electrostatic potential (ESP) are computed from the positions of the atomic nuclei and the electron density of molecules. From the ESP maps, the high extent and lack of electrons in different parts of the molecular structures are shown to target the reactive positions of the molecules. Fig. 4. shows the ESP map of the  $\text{Fe}_3\text{O}_4/\text{PTh}$  nanocomposite. The low electrostatic potential values (negative charge) are in red and the high electrostatic potential energies (positive charge) are in blue color.

As can be seen, the PTh is positively charged (blue colors) and the  $\text{Fe}_3\text{O}_4$  molecule is negatively charged (red colors) in ESP isosurface. It shows that charge is transferred from the PTh to  $\text{Fe}_3\text{O}_4$ , which is in agreement with the Mulliken charge transfer result.

### 3.2. Effect of variable features on adsorption process

#### 3.2.1. Effect of solution pH

The solution pH is one of the key parts in the adsorption process. This is due to the fact that the transfer reactions of protons are responsible for controlling the surface charge of adsorbents, which are located between the solution and the solid surface, and in the various pHs can be positive, negative or close to zero [34]. Furthermore, it affects the protonation of surface groups, the extent of ionization, and the speciation of the adsorbates [35]. The influence of initial solution pH on Pb(II) removal efficiency and adsorption capacity by the  $\text{Fe}_3\text{O}_4/\text{PTh}$  nanocomposite from pH 2 to 6 at ambient temperature is shown in Fig. 5a. Our results showed that Pb(II) ions removal by  $\text{Fe}_3\text{O}_4/\text{PTh}$  nano-adsorbent enhanced with the increasing pH values and adsorption process is strongly pH-dependent. Both removal percent and adsorption capacity soared and from 67.42% and 3.371 mg/g (at pH 2) reached to 90.98% and 4.549 mg/g (at pH 6), respectively. Firstly, in the lower pH region, the rival

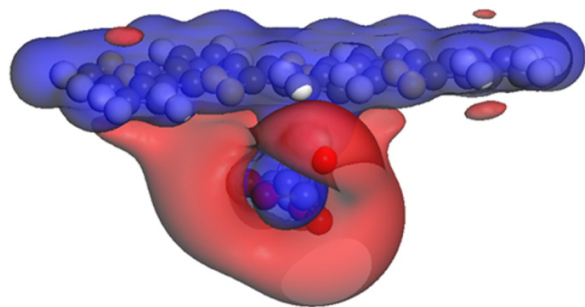


Fig. 4. Calculated electrostatic potential surface (ESP) of  $\text{Fe}_3\text{O}_4/\text{PTh}$ . The red color is referred to the negative sites and the blue one is referred to the low electron density.

between the  $\text{H}^+$  ions and Pb(II) cations for the adsorption on the flowing sites of magnetic nano-sorbent is the reason of less adsorption. Domination of the positively charged sites is an equally significant aspect, this causes the enhancement of the repulsion forces existing between the sorbent surface and the Pb(II) ions, and in this manner decreases the adsorption of Pb(II) ions. With an increase in pH, the deprotonation of sorbent surface eventuate in the increase of the negatively charged sites and subsequently adsorption process is facilitated by increasing attractive forces between the sorbent surface and the Pb(II) ions [36], It could also be said that reducing  $\text{H}^+$  concentration in higher pH results easier mass transfer for Pb(II) ions.

#### 3.2.2. Effect of adsorbent dose

The addition of different values of  $\text{Fe}_3\text{O}_4/\text{PTh}$  (from 2.5 to 20 g  $\text{L}^{-1}$ ) to 10 mL of lead solution at room temperature was the initial step to discover the sufficient amount of adsorbent to achieve the highest possible interactions between Pb(II) ions and adsorption sites of adsorbent in the solution and consequently maximum adsorption capacity. As can be seen in Fig. 5b, with growing adsorbent dose from 2.5 g to 20 g, the removal efficiency elevated from 44.4% to 91.42% and adsorption capacity decline from 8.88 mg/g to 2.28 mg/g. Removal percent increased up to 100 g dose and beyond the optimum dose, there was no significant change. This finding was predictable since for a fixed initial concentration, increasing adsorbent dose results in higher number of free active sites for adsorption, where adsorbed metal ions quantity ( $q_e$ ) per unit weight of the sorbent decreases following the increase in the  $\text{Fe}_3\text{O}_4/\text{PTh}$  nano-sorbent quantity.

#### 3.2.3. Effect of initial metal ions concentration

The process of adsorption was conducted under multiple concentrations (from 50 mg  $\text{L}^{-1}$  to 400 mg  $\text{L}^{-1}$ ) so that the effect of initial Pb(II) concentration on the adsorption of metal ions and isotherm studies could be investigated. Fig. 5c shows a negative correlation in which the increment of initial metal ions concentration results in the decrement of removal efficiency from around 90.98% at 50 mg  $\text{L}^{-1}$  to 77.97% at 400 mg  $\text{L}^{-1}$  and, contrariwise, adsorption capacity of metal ions on the  $\text{Fe}_3\text{O}_4/\text{PTh}$  nanoparticles move in the same direction with initial metal ions from 4.549 mg/g to 31.19 mg/g. Decreasing removal efficiency can be attributed to occupying the surface sites of  $\text{Fe}_3\text{O}_4/\text{PTh}$  nano sorbent and elevating repulsive forces at higher concentration. Increasing adsorption capacity can be related to the lower possibility of all the surface sites of  $\text{Fe}_3\text{O}_4/\text{PTh}$  nano-adsorbent being occupied.

#### 3.2.4. Effect of contact time

The optimum removal efficiency could be achieved by obtaining the equilibrium time of Pb(II) adsorption. To this end, the dependence of removal efficiency to contact time was investigated. The removal efficiency and amount of Pb(II) adsorbed onto  $\text{Fe}_3\text{O}_4/\text{PTh}$  is indicated as a function of time in Fig. 5d. The removal efficiency changed from 33.47% in 5 min to 90.34% when contact time was 60

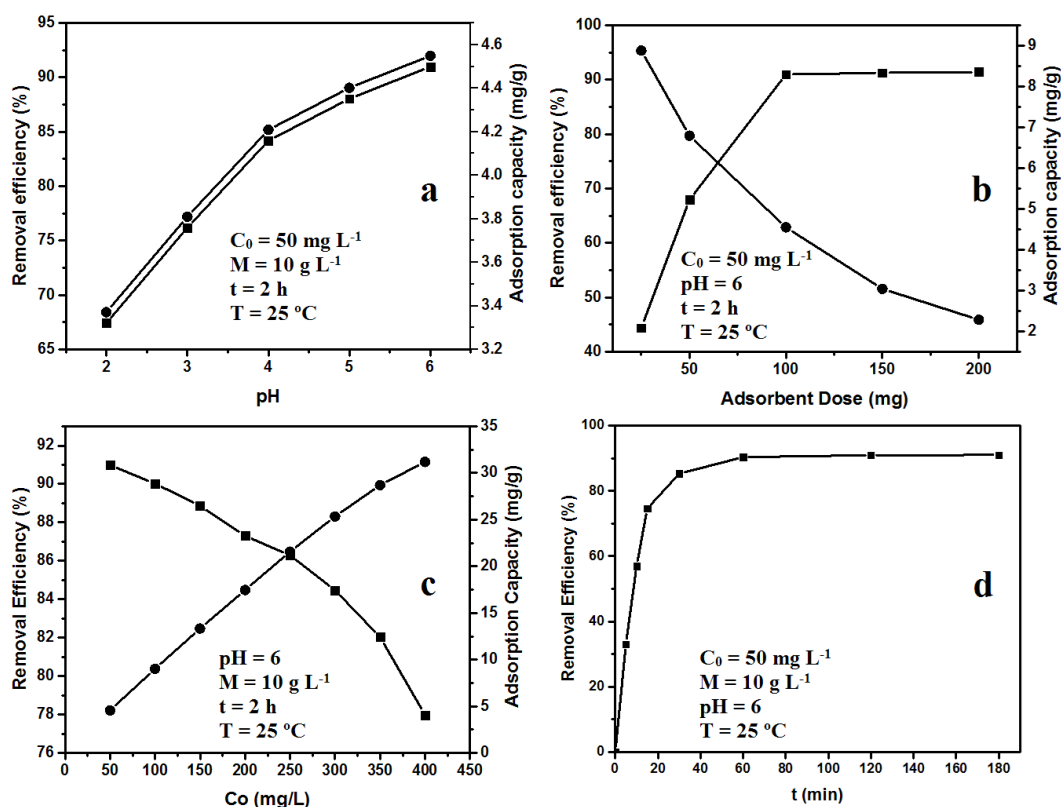


Fig. 5. Effects of operating condition, pH solution (a) adsorbent dose (b), initial concentration (c) and contact time (d) on removal efficiency -■- and adsorption capacity -●-.

min and after 60 min, these values remained practically unchanged that showed the establishment of equilibrium condition. Consequently, the most favorable contact time was 60 min for sorption of Pb(II) by Fe<sub>3</sub>O<sub>4</sub>/PTh nanoparticles. The rapid sorption of Pb(II) pending the first minutes (<5 min) can be the result of the high availability of active sites on the fresh Fe<sub>3</sub>O<sub>4</sub>/PTh surface. The removal efficiency rate undergoes a slow decrement overtime in the adsorption process and keeps on decreasing to the equilibrium. The decrement of Pb(II) adsorption rate can be attributed to the slow pore diffusion of Pb(II) ions into the bulk of Fe<sub>3</sub>O<sub>4</sub>/PTh.

### 3.3. Kinetic studies

Systematic evaluation of the adsorption process requires some kinetic models to analyze the rate data. Kinetic parameters of Pb(II) adsorption on the Fe<sub>3</sub>O<sub>4</sub>/PTh are determined by applying kinetic models including the pseudo-first-order and pseudo-second-order in two ways linear and nonlinear. The correspondence between experimental data and the obtained amounts of the model was provided by the correlation coefficient (R<sup>2</sup>). The obtained R<sup>2</sup> values (close or equal to 1) show the success of the proposed model in explaining the kinetics of Pb(II) adsorption.

The pseudo-first-order model is based on the hypothesis that the rate is proportional to the number of unoccupied sites and the amount of adsorption corresponding to mono-

layer coverage [37]. The nonlinear and linear form of this model is shown in Eqs. (5) and (6), respectively:

$$q_t = q_e (1 - e^{-k_1 t}) \quad (5)$$

$$\ln(q_e - q_t) = \ln q_e - k_1 t \quad (6)$$

where  $q_e$  and  $q_t$  (mg/g) represent the amount of Pb(II) adsorbed onto the adsorbent at equilibrium and at time  $t$ , respectively, and  $k_1$  is the first-order adsorption rate constant (min<sup>-1</sup>).

In pseudo-second-order model, chemical adsorption is the main factor controlling the reaction rate, where the removal from a solution is due to exchange or sharing of electrons between adsorbate and the binding sites on adsorbent [38]. The nonlinear and linear form of this model is indicated in Eqs. (7) and (8), respectively:

$$q_t = \frac{q_e^2 k_2 t}{1 + q_e k_2 t} \quad (7)$$

$$\frac{t}{q_t} = \frac{1}{k_2 q_e^2} + \left( \frac{1}{q_e} \right) \times t \quad (8)$$

where  $k_2$  is the second-order rate constant (g mg<sup>-1</sup>/min) for the adsorption process, and  $q_e$  is the adsorption amount obtained from the pseudo-second-order kinetic model (mg/g).

The plots of Eqs. (5), (6), (7) and (8) are indicated in Figs. 6a, b, c, and d, respectively. The data used in this

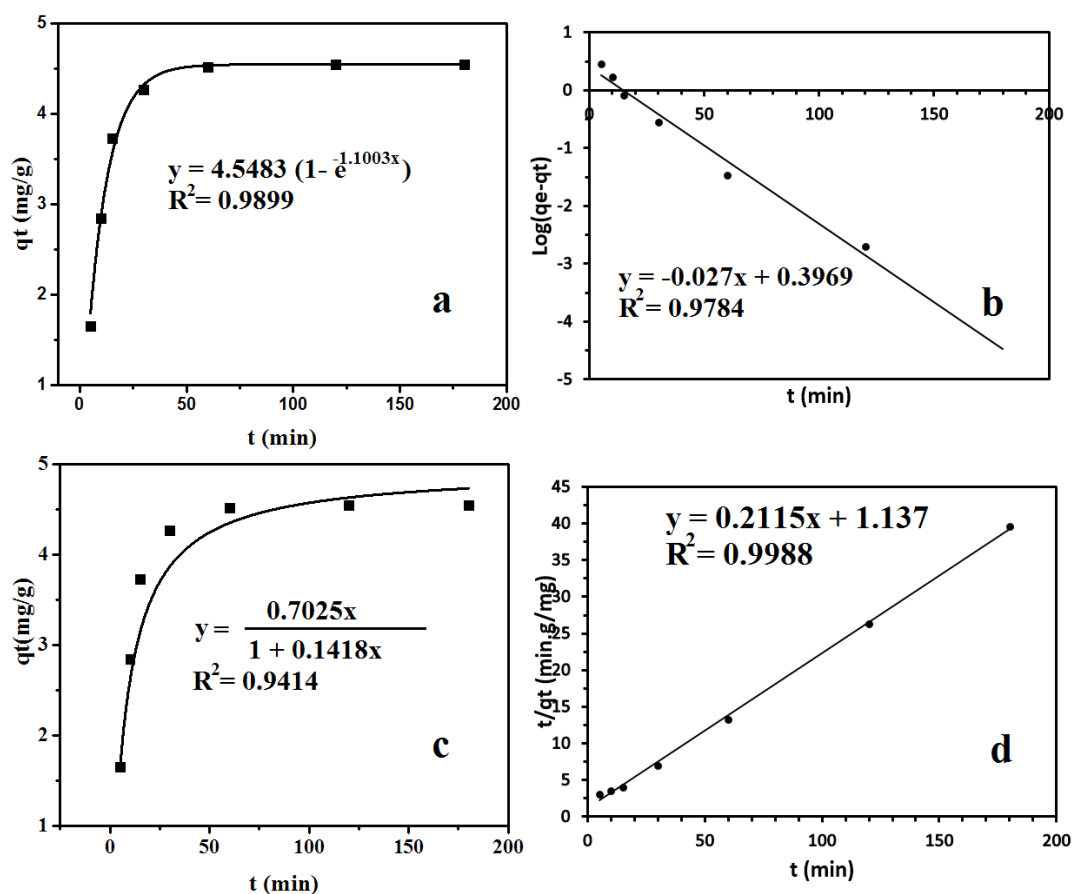


Fig. 6. Adsorption kinetic curves of  $Pb^{2+}$  ions by magnetite/polythiophene adsorbents at initial concentration =  $50 \text{ mg L}^{-1}$ , adsorbent dose =  $10 \text{ g L}^{-1}$ , pH = 6 and  $T = 25^\circ\text{C}$  pseudo-first-order (a), linearized pseudo-first-order (b), pseudo-second-order (c) and linearized pseudo-second-order (d).

section is obtained from the effect of contact time. The obtained kinetic constants and correlation coefficients from the plots are shown in Table 2. According to the obtained amounts of the correlation coefficients, the linearized pseudo-second-order model ( $R^2 \approx 0.9998$ ) is more successful in explaining the  $Pb(II)$  adsorption than the other models. In addition, the obtained value of  $q_e$  from the pseudo-second-order model is almost close to the experimental values.

### 3.4. Isothermal studies

The study of equilibrium adsorption isotherm is an undeniable part of the creation and operation of the adsorption systems. Equilibrium studies in adsorption provide sufficient information about the sorption mechanism, the surface properties and capacity of the adsorbent. Equilibrium relationships between adsorbent and adsorbate, called adsorption isotherms, is mainly related to the ratio between the concentration of lead in solution and the amount of lead adsorbed on adsorbent at a fixed temperature when both the phases are at equilibrium. The Langmuir, Temkin, Freundlich, Sips, and Redlich-Peterson isotherm models were investigated in the current study to explain the equilibrium experimental data.

Table 2

Computed kinetic parameters for  $Pb(II)$  adsorption on  $Fe_3O_4/PTH$  nanoparticles

Pseudo-first-order model			
	$K (\text{min})^{-1}$	$q_e (\text{mg}\cdot\text{g}^{-1})$	$R^2$
Nonlinear	0.1003	4.5483	0.9899
Linear	0.062	2.49	0.9784
Pseudo-second-order model			
	$K (\text{g}\cdot\text{mg}^{-1}\cdot\text{min}^{-1})$	$q_e (\text{mg}\cdot\text{g}^{-1})$	$R^2$
Nonlinear	0.0286	4.954	0.9414
Linear	0.039	4.728	0.9988

The Langmuir model explains adsorptions on a surface that has a relatively small number of similar and equivalent binding energy and there is a basic assumption that predicts the single layer coverage of the adsorbate on the outer surface of the adsorbent. Furthermore, the model proposes that the energy of adsorption is constant, the adsorbate molecules do not interact with the surface. Moreover, the adsorbent surface is also homogenous which helps the adsorbent sites connect with molecules

that have the highest adsorbate rate. This isotherm model is presented by Eq. (9):

$$q_e = q_m \frac{K_L C_e}{1 + K_L C_e} \quad (9)$$

where  $q_e$  is the amount of Pb(II) adsorbed per specific amount of adsorbent (mg/g),  $C_e$ , the equilibrium concentration of the solution (mg L<sup>-1</sup>),  $q_m$ , the maximum amount of monolayer adsorption metal ions (mg/g) and  $K_L$  is the Langmuir constant associated with the energy of adsorption. We can rearrange this equation into the linear type that is represented by Eq. (10):

$$\frac{C_e}{q_e} = \frac{1}{q_m K_L} + \frac{1}{q_m} C_e \quad (10)$$

By plotting the nonlinear graph of  $q_e$  against  $C_e$ , the values of  $K_L$ , and  $q_m$  are determined from the obtained equation by Fig. 7a. In linearized type  $C_e/q_e$  is plotted against  $C_e$  and the values of  $K_L$  and  $q_m$  can be determined from the intercept and slope of the Fig. 7b. As it is illustrated in Table 3, the values of  $q_m$  and  $K_L$  are 46.49 mg/g and 0.0246 L mg<sup>-1</sup> in nonlinear form and 46.51 and 0.0243 in linear form.

Furthermore, the favorability properties and efficiency of Langmuir isotherm in a dimensionless constant separation factor  $R_L$  is given as:

$$R_L = \frac{1}{1 + K_L C_i} \quad (11)$$

where  $K_L$  is the Langmuir constant (L mg<sup>-1</sup>) and  $C_i$  is the highest initial Pb(II) concentration and values between 0 and 1 imply favorable adsorption. In the present investigation, the value of  $R_L$  was calculated to be 0.093 which indicates practicable adsorption of Pb(II) onto Fe<sub>3</sub>O<sub>4</sub>/PTH nanoparticles surface.

The Freundlich equation is the simplest heterogeneous model and strictly empirical. The equation of this data-driven model can be obtained according to the sorption on the non-uniform surface in which the enthalpy of adsorption experiences a logarithmic decline as the fraction of occupied sites is considered. Recently, Freundlich isotherm has been criticized because it had no thermodynamic basis and this model doesn't approach Henry law in low concentrations [39]. Its non-linearized and linearized equations are presented in Eqs. (12) and (13), respectively:

$$q = K_f C_e^n \quad (12)$$

$$\ln(q) = \ln(K_f) + n \ln(C_e) \quad (13)$$

where  $K_f$  (mg/g)(dm<sup>3</sup>/g)<sup>n</sup> and  $n$  constants stand for the adsorption capacity and intensity of adsorption, respectively. The values of the constant  $n$ ,  $K_f$  and  $R^2$  were calculated from the equations derived from the graphs in Figs. 7c and d and represented in Table 3.

The assumption considered in Temkin isotherm is in compliance with this phenomenon that adsorption heat in all molecules in the layer would have linear decline with coverage through passing over the remarkably low and high value of concentrations. This equation is based on the estimation that the gas phase equilibrium is established;

however, the complex adsorption systems including the liquid-phase adsorption isotherms are not appropriate [39]. The Temkin nonlinear and linear equation model is expressed as:

$$q_e = \frac{RT}{b} \ln(A_T C_e) \quad (14)$$

$$q_e = B_T \ln(A_T) + B_T \ln(C_e) \quad (15)$$

where  $R$  is the universal gas constant (8.314 J/Kmol),  $T$ , the absolute temperature (K), and  $b$  and  $A_T$  represent constant related to the heat of sorption (J/mol) and Temkin isotherm equilibrium binding constant (L/g), respectively. Table 3 shows the calculated  $A_T$ ,  $B_T$  and  $R^2$  from the Temkin model.

The three empirical parameters Redlich–Peterson isotherm contains the properties of the Langmuir and Freundlich equations. This isotherm has a linear dependence on concentration in the numerator and a nature of *exponential functions* in the denominator. Moreover, it is close to Henry's law at low concentrations and its behavior looks like the Freundlich isotherm at high concentrations [40]. There are two possible systems to use the hybrid isotherm for versatility: homogeneous or heterogeneous. Non-linear and linear type of Redlich–Peterson isotherm can be described as:

$$q_e = \frac{K_R C_e}{1 + a_R C_e^{b_R}} \quad (16)$$

$$\log\left(K_R \frac{C_e}{q_e} - 1\right) = b_R \log C_e + \log a_R \quad (17)$$

where  $K_R$  is the Redlich–Peterson adsorption capacity constant (L g<sup>-1</sup>), the parameter  $a_R$  is also having a constant unit of (L mg<sup>-1</sup>)<sup>b<sub>R</sub></sup>,  $b_R$  is an exponent that lies between 0 and 1. When  $b_R$  tends to 1, the R-P equation becomes the Langmuir isotherm equation and when  $b_R$  is all close to 0, it is in accordance with the Freundlich equation but the accuracy of these interpretations strongly depends on the fitting method [41]. In solving the linearized equation, a minimization procedure is applied by increasing the correlation coefficient between the experimental data points and theoretical model predictions with Matlab R2009a. The values of  $a_R$ ,  $b_R$ ,  $K_R$  and  $R^2$  are indicated in Table 3.

Sips isotherm is a mixture of the Langmuir and Freundlich isotherms that considers the heterogeneity and bypasses the limitation of the increasing adsorbate concentration related to the Freundlich isotherm model. The adsorbate concentration changes its behavior in lower values as it decreases to Freundlich isotherm. In contrast, the high concentrations promise a monolayer adsorption capacity of the Langmuir isotherm [42]. The Sips isotherm and its linearized can be given as follows:

$$q_e = \frac{Q_{\max} (K_S C_e)^{1/n_s}}{1 + (K_S C_e)^{1/n_s}} \quad (18)$$

$$\frac{1}{q_e} = \frac{1}{Q_{\max} K_S} \left( \frac{1}{C_e} \right)^{1/n_s} + \frac{1}{Q_{\max}} \quad (19)$$

where  $K_S$  (1/mg),  $Q_{\max}$  (mg/g) and  $n_s$  are the affinity constant, maximum adsorption capacity and dimensionless

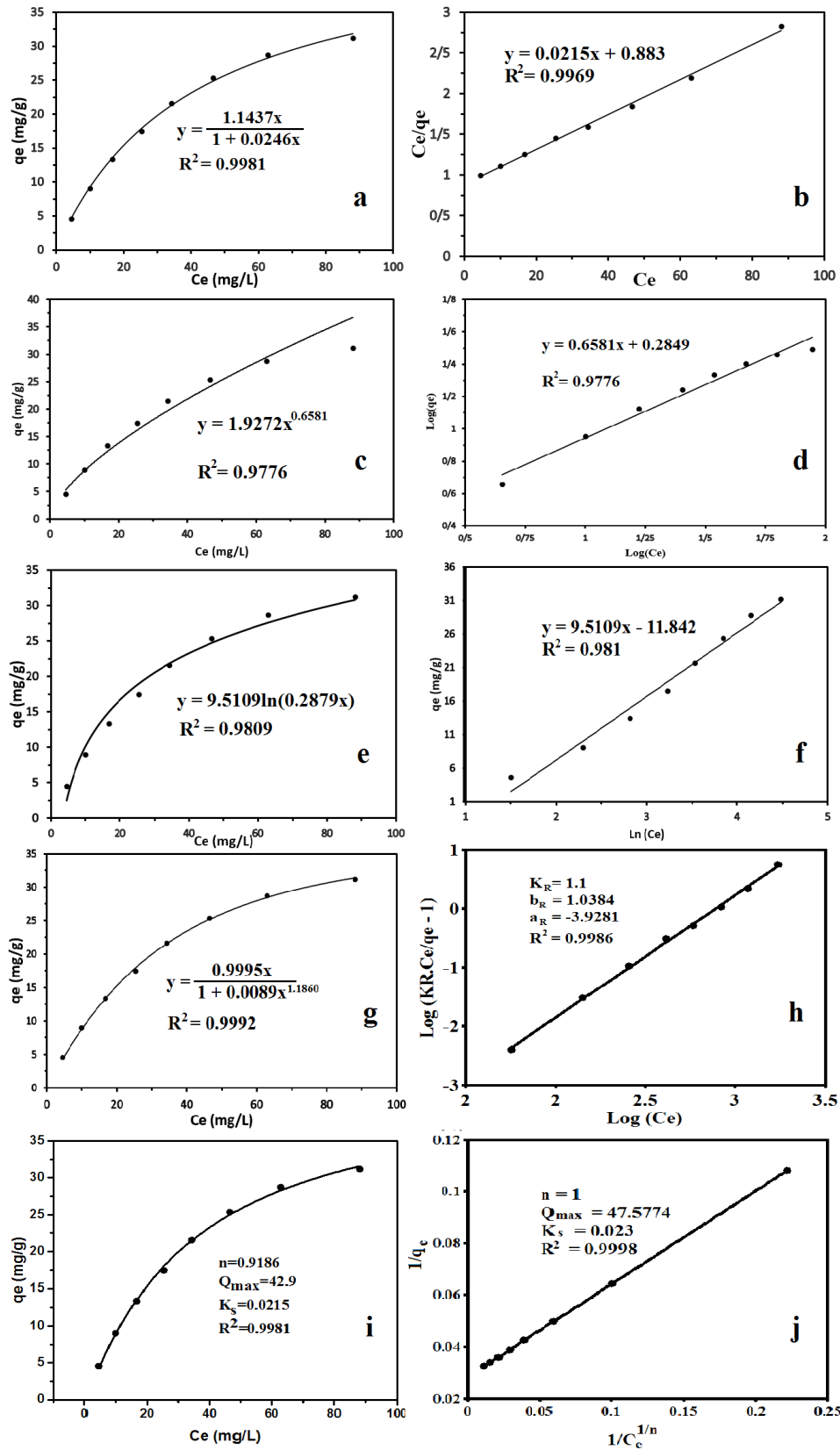


Fig. 7. Adsorption isotherms curves of  $Pb^{2+}$  ions by magnetite/polythiophene adsorbents at adsorbent dose =  $10 \text{ g L}^{-1}$ , pH = 6 and  $T = 25^\circ\text{C}$ , Langmuir (a), linearized Langmuir (b), Freundlich (c) linearized Freundlich (d), Temkin (e), linearized Temkin (f), Redlich-Peterson (g), linearized Redlich-Peterson (h), Sips (i) linearized Sips (j).

Table 3  
Adsorption parameters of the isotherm models for the adsorption of Pb<sup>2+</sup> ions onto Fe<sub>3</sub>O<sub>4</sub>/PTh nanocomposite

Adsorption model	Langmuir			Freundlich			Temkin		
	R <sup>2</sup>	q <sub>max</sub> (mg·g <sup>-1</sup> )	K <sub>L</sub> (L/mg)	R <sup>2</sup>	1/η	k <sub>f</sub> (mg·g <sup>-1</sup> )(l/mg) <sup>1/η</sup>	R <sup>2</sup>	B <sub>T</sub>	K <sub>T</sub> (L/mg)
Linear	0.9981	46.49	0.0246	0.9776	1.52	1.93	0.9809	9.5109	0.2879
Nonlinear	0.9969	46.51	0.0243	0.9776	1.52	1.33	0.981	9.511	0.2879
	Redlich-Peterson			Sips					
	R <sup>2</sup>	b <sub>R</sub>	a <sub>R</sub> (1/mg)	R <sup>2</sup>	q <sub>max</sub> (mg·g <sup>-1</sup> )	K <sub>S</sub> (L/g)			
Linear	0.9986	1.0348	0.0196	0.9981	42.9	0.0215			
Nonlinear	0.9992	1.1860	0.0089	0.9998	47.577	0.023			

Table 4  
Comparison of maximum adsorption capacity of Fe<sub>3</sub>O<sub>4</sub>/PTh with those of some other adsorbents reported in literature for Pb<sup>2+</sup> adsorption

Adsorbents	pH	Temperature (°C)	Isotherm	Q <sub>m</sub> (mg/g)	Ref
Hollow magnetite nanospheres	5	25	Langmuir	13.40	[43]
TiO <sub>2</sub> functionalized with hydroxide ethyl aniline (PHEA/n-TiO <sub>2</sub> )	5.5	55	Langmuir	26.05	[44]
Fe <sub>3</sub> O <sub>4</sub> /cyclodextrin polymer	5.5	25	Langmuir	64.50	[45]
Fe <sub>3</sub> O <sub>4</sub>	5.5	55	Freundlich	36.0	[36]
Thiosemicarbazide modified chitosan	5	55	Langmuir	56.89	[46]
Chitosan immobilized on bentonite	4	25	Freundlich	26.38	[47]
Activated carbon– calcium alginate	5	25	Langmuir	15.7	[48]
γ-Fe <sub>2</sub> O <sub>3</sub> - alginate beads	7	30	Langmuir	50	[49]
Fe <sub>3</sub> O <sub>4</sub> /powder activated carbon	6	25	Langmuir	80	[50]
Fe <sub>3</sub> O <sub>4</sub> /PTh	6	25	Sips	47.5	[Present study]

heterogeneity factor, respectively. The surface heterogeneity factor,  $n_s$ , is between 0 and 1. When  $n_s$  will be close to 1, the Sips equation decreases to the Langmuir equation and it implies a homogeneous adsorption process [42]. Aforesaid parameters are depicted in Table 3. In linear type, a trial and error procedure has been applied to find the maximum value of the correlation coefficient by varying  $n_s$ . Then values of  $K_s$  and  $R^2$  are obtained from the slope and the intercept of the plot in Fig. 7.

As depicted, the curves of Eqs. (9), (10), (12), (13), (14), (15), (16), (17), (18) and (19) are shown in Fig. 7 and the isotherm constants and correlation coefficients for nonlinear and linear Langmuir, Freundlich, Temkin, Redlich-Peterson, and Sips equations are listed in Table 3. The each nonlinear and linear Freundlich model clearly shows poor correlation ( $R^2 = 0.9776$ ) to the experimental data. Similarly, the Temkin isotherm model that predicts a drop in the temperature of sorption is linear rather than logarithmic, does not fit well with the experimental data ( $R^2 = 0.981$ ). In this way, it can be understood that the Pb<sup>2+</sup> adsorption using Fe<sub>3</sub>O<sub>4</sub>/PTh adsorbent was not really a chemical adsorption process. All the Langmuir ( $R^2 = 0.9981$  and  $0.9969$  for nonlinear and linear form, respectively), Redlich-Peterson ( $R^2 = 0.9992$  and  $0.9986$  for nonlinear and linear form, respectively) and Sips isotherm ( $R^2 = 0.9981$  and  $0.9998$  for nonlinear and linear form, respectively) models show a good fit to experimental data. Furthermore, homogeneous adsorption

process is evidently indicated by the heterogeneity factor value ( $n = 1$  in linear Sips equation and  $b_R = 1.186$  in the nonlinear Redlich-Peterson equation). The adsorption isotherm data on this adsorbent are better fitted to linear Sips isotherm model ( $R^2 = 0.9998$ ) compared to other models and calculated maximum adsorption capacity by linear Sips equation was 47.577 mg/g. Table 4 summarizes the maximum adsorption capacity of several adsorbents taken from the literature with Fe<sub>3</sub>O<sub>4</sub>/PTh nanocomposite in this study. From the results, it is found that the Fe<sub>3</sub>O<sub>4</sub>/PTh nanocomposite has a relatively good and satisfactory potential and can be considered as a promising adsorbent for the removal of Pb(II) from industrial wastewater.

### 3.5. Thermodynamic study

#### 3.5.1. Effect of temperature on adsorption of Pb(II)

To investigate the effects of temperature, adsorption experiments were studied in 25°C, 30°C, 45°C, and 60°C at optimum conditions in 10 mL of solutions with the initial concentration of 50 mg L<sup>-1</sup> of Pb(II), the adsorbent dose of 0.1 g, optimum pH (pH = 6) and equilibrium contact time 60 min. As can be seen in Fig. 8a, when the temperature rises from 25°C to 60°C, Pb<sup>2+</sup> ions removal efficiency increases reaching up to 100% at the temperature 60°C. This phenomenon ascertains the endothermic nature of the adsorption.

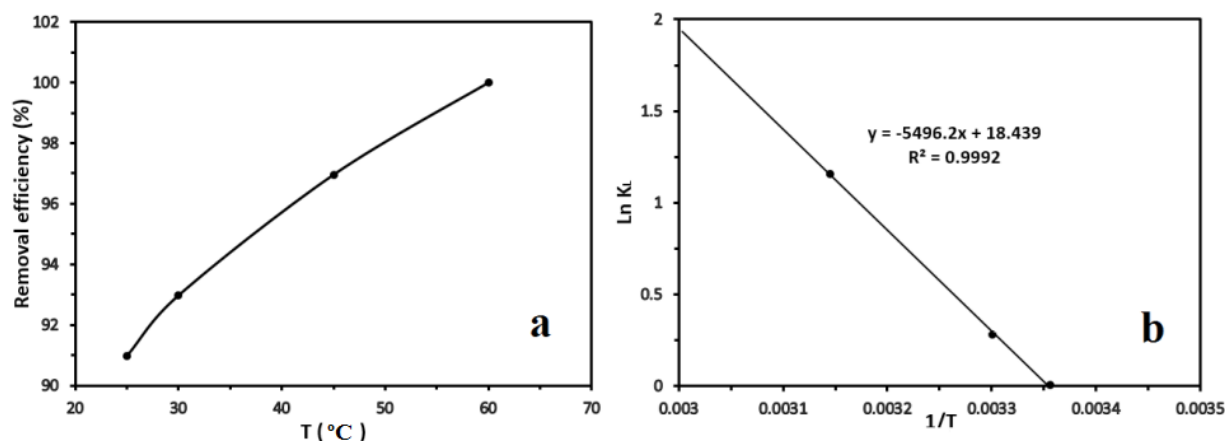


Fig. 8. Effect of temperature on Pb(II) removal (a) obtained curve from Van 't Hoff equation (b).

It can be more explained that, before adsorption process, Pb(II) ions in solution are surrounded by water ions, these ions need to increase their energy to release themselves and get to adsorbent surface during the adsorption process.

### 3.5.2. Evaluation of thermodynamics parameter

Using the results obtained in the last section, the thermodynamic parameters such as difference in standard Gibbs free energy ( $\Delta G^\circ$ ), entropy ( $\Delta S^\circ$ ) and enthalpy ( $\Delta H^\circ$ ) for the adsorption of Pb(II) by the  $\text{Fe}_3\text{O}_4/\text{PTh}$  were determined and also significant information on the type of process were provided. These parameters were calculated from Eqs. (20)–(23):

$$\Delta G^\circ = -RT \ln K \quad (20)$$

$$K = \frac{q_e}{C_e} \quad (21)$$

$$\Delta G^\circ = \Delta H^\circ - T \Delta S^\circ \quad (22)$$

$$\ln K = \frac{\Delta S^\circ}{R} - \frac{\Delta H^\circ}{RT} \quad (23)$$

where  $\Delta S^\circ$ ,  $\Delta H^\circ$ , and  $\Delta G^\circ$  are the changes of entropy (kJ/mol), enthalpy (kJ/mol) and Gibbs free energy (kJ/mol·K), T is the absolute temperature (K), R is the universal gas constant ( $8.314 \times 10^{-3}$  kJ/mol·K) and K is the distribution coefficient for the adsorption. As indicated in Fig. 8b, by plotting of  $\ln K$  vs.  $1/T$ , the values of  $\Delta H$  and  $\Delta S$  were obtained using the slopes and intercepts. Thermodynamic parameters for the adsorption process gained from Eqs. (20)–(23) and Fig. 8b and are listed in Table 5. As shown in Table 5, the negative value of  $\Delta G^\circ$  at all temperatures shows the spontaneous nature and the thermodynamically favorable of Pb(II) adsorption onto  $\text{Fe}_3\text{O}_4/\text{PTh}$  nanoparticles. The further negative value of  $\Delta G^\circ$  after an increase in temperature implies that the driving force of adsorption is directly proportional to the temperature. A further point to be considered that  $\Delta G^\circ$  values between  $-20$  and  $0$  kJ/mol imply spontaneous physical process, whereas that values between  $-80$  and  $-400$  kJ/mol imply chemisorptions. Consequently, it can be found that the adsorption mechanism in this study is dominated

Table 5

Thermodynamic parameters for Pb(II) adsorption on  $\text{Fe}_3\text{O}_4/\text{PTh}$  nanoparticles

Temperature (K)	$\Delta G^\circ$ (kJ·mol <sup>-1</sup> )	$\Delta H^\circ$ (kJ·mol <sup>-1</sup> )	$\Delta S^\circ$ (kJ·K <sup>-1</sup> mol <sup>-1</sup> )
298	-0.021	45.69	0.153
303	-0.705		
318	-3.066		
333	-		

Table 6

Obtained results of reproducibility experiments for adsorption/elution processes for Pb(II) ions by  $\text{Fe}_3\text{O}_4/\text{PTh}$  nanocomposite

Cycle	Removal efficiency (%)	Adsorption capacity (mg·g <sup>-1</sup> )
I	90.98	4.549
II	90.24	4.512
III	88.93	4.447
IV	85.72	4.286
v	80.32	4.016

by physisorption. As expected, the value of  $\Delta H^\circ$  is positive suggesting the endothermic nature of the sorption process. The  $\Delta H^\circ$  obtained value 45.69 kJ/mol indicates that sorption process happens on the verge of physical and chemical adsorption as seen from the  $\Delta G^\circ$  analysis. The positive value of  $\Delta S^\circ$  reflected that the system exhibits random behavior due to releasing water ions by lead ions during the adsorption process.

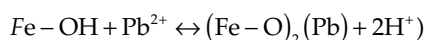
### 3.6. Desorption and reusability

One of the important procedures in the wastewater treatment systems through adsorption process is evaluating regeneration of the adsorbent and possibility of adsorbate desorption. As mentioned before, the reusability of the adsorbent was evaluated by repeating the adsorption-desorption cycles of Pb(II) for five times by reusing the spent

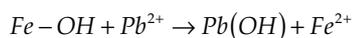
adsorbent. Table 6 presents no significant change in the removal efficiency and adsorption capacity during three adsorption-desorption cycles. In the fourth and fifth cycles, the obtained values were also favorable. Based on the findings, the adsorption process was reversible and  $\text{Fe}_3\text{O}_4/\text{PTh}$  nanoparticles were able to be used for multiple time to extract heavy metal ions from wastewater. To confirm the integrity of  $\text{Pb}^{2+}$  adsorption on nanocomposite, EDX analysis was done before and after adsorption process and the results are summarized in Fig. 9. It can be seen that the peak of Pb appear in magnetite/PTh, indicating that the  $\text{Pb}(\text{II})$  ions exist on the nanoparticles.

### 3.7. Adsorption mechanism

The PTh has a reactive S atom in a polymer chain. It goes through two main processes of protonation and deprotonation during adsorption processing because of having two lone pairs of electrons. Protonation of PTh maintains charge neutrality by acquiring of protons and also anions. Therefore, the dominant adsorption positions for  $\text{Pb}(\text{II})$  ions are the sulfur atoms in the macromolecular polymeric chains. This performance is because of the properties of sulfur atom with single pairs of electrons that can proficiently bind a metal ion to form a metal complex [51]. Also, there is possibility the involvement of O atoms of the magnetite in the adsorption process which is through electrostatic attraction between  $\text{Pb}^{2+}$  ions (positive dipole) and oxygen functionalities  $\text{Fe}_3\text{O}_4$  nanoparticles (negative dipole) occurs [52]. Processes such as anion exchange and hydrolysis have associated in heavy metal ions removal. A potential mechanism of anions and heavy metal ions adsorption onto the  $\text{Fe}_3\text{O}_4/\text{PTh}$  nanocomposite can be related to exchange of  $\text{H}^+$  ions with  $\text{Pb}^{2+}$  on the surface of magnetite hydroxyl groups  $-\text{Fe}'\text{OH}$  [43]:



The following equation can be also used for illustrating the ion exchange process [53]:



### 3.8. DFT study of adsorption behavior

To find the most stable  $\text{Pb}$ -adsorbed structure of  $\text{Fe}_3\text{O}_4/\text{PTh}$ , two initial configurations were used for full structural optimization, including  $\text{Pb}(\text{II})$  adsorption on the surface of PTh or on the side of the  $\text{Fe}_3\text{O}_4$  molecule. Our calculation results show that the  $\text{Pb}$  can be adsorbed with adsorption energies of  $-0.55\text{eV}$  ( $-53.44\text{ kJ/mol}$ ) and  $-2.82\text{eV}$  ( $-272.11\text{ kJ/mol}$ ) on the surface of PTh and  $\text{Fe}_3\text{O}_4$  of the nanocomposite, respectively. The calculated electronic energy of two adsorption configuration shows that the structure of  $\text{Pb}$  adsorption near the magnetite molecule is more stable energetically ( $2.27\text{eV}$ ) rather than other adsorption configuration.

The  $E_{ad}$  values show that  $\text{Pb}(\text{II})$  prefers to be adsorbed on the side of the  $\text{Fe}_3\text{O}_4$  molecule which confirms the ESP map results. The analyses of ESP revealed that the magnetite in nanocomposite is the reactive site (negative charge) for effective adsorption of  $\text{Pb}^{2+}$ . Fig. 10a shows the most stable configuration of  $\text{Pb}$ -adsorbed  $\text{Fe}_3\text{O}_4/\text{PTh}$  nanocomposite.

The obtained results from this optimized adsorption structure (Fig. 10a) show that the closest interaction distances of  $\text{Pb}$  and O atoms of magnetite are about  $2.2\text{Å}$ , which agrees well with the  $\text{Pb}-\text{O}$  single bond lengths of oxido-hydroxido complexes of  $\text{Pb}(\text{II})$  in a previous study [54].

Investigations the adsorption geometries show that the  $\text{Pb}$  adsorption induces insignificant changes in bond lengths and angles of the  $\text{Fe}_3\text{O}_4/\text{PTh}$  nanostructure. Our calculation results show that in adsorption process the HOMO and LUMO energy levels change slightly and the energy gap increases from  $0.5\text{eV}$  for pristine  $\text{Fe}_3\text{O}_4/\text{PTh}$  to  $0.69\text{eV}$  in  $\text{Pb}$ -adsorbed form.

To explain the influence of the  $\text{Pb}$  adsorption on the  $\text{Fe}_3\text{O}_4/\text{PTh}$  electronic properties, the current study has investigated the distribution of the frontier molecular orbitals including the HOMO and LUMO of the pristine nanocomposite and the most stable  $\text{Pb}$ -adsorbed configuration. Fig. 10b illustrates the spatial distribution of HOMO and the LUMO of the pristine  $\text{Fe}_3\text{O}_4/\text{PTh}$  and the adsorption structure.

As can be seen in Fig. 10b in  $\text{Fe}_3\text{O}_4/\text{PTh}$  the HOMO and LUMO are mainly localized on the magnetite molecule. When the  $\text{Pb}$  is adsorbed on the nanocomposite sur-

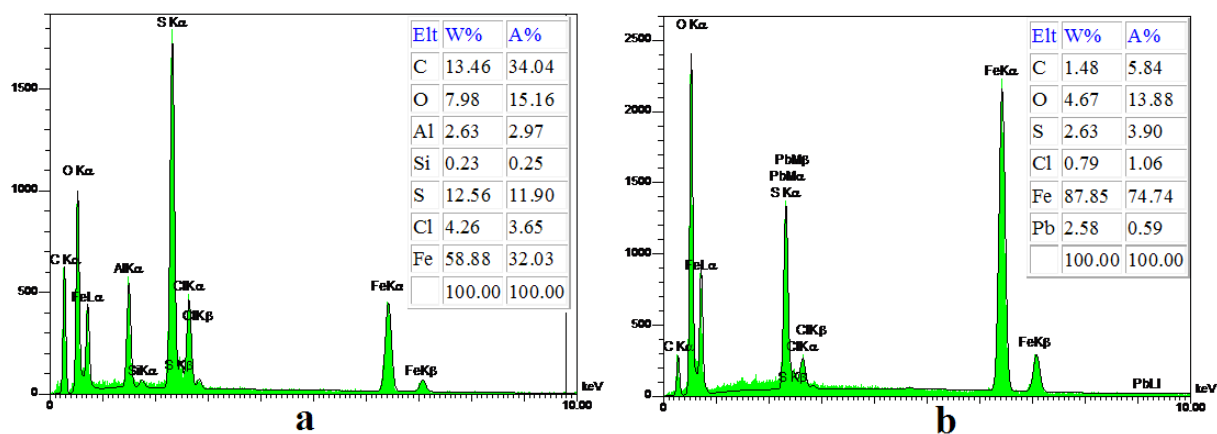


Fig. 9. EDX spectra of  $\text{Fe}_3\text{O}_4/\text{PTh}$  nanocomposite before (a) and after (b)  $\text{Pb}(\text{II})$  adsorption.

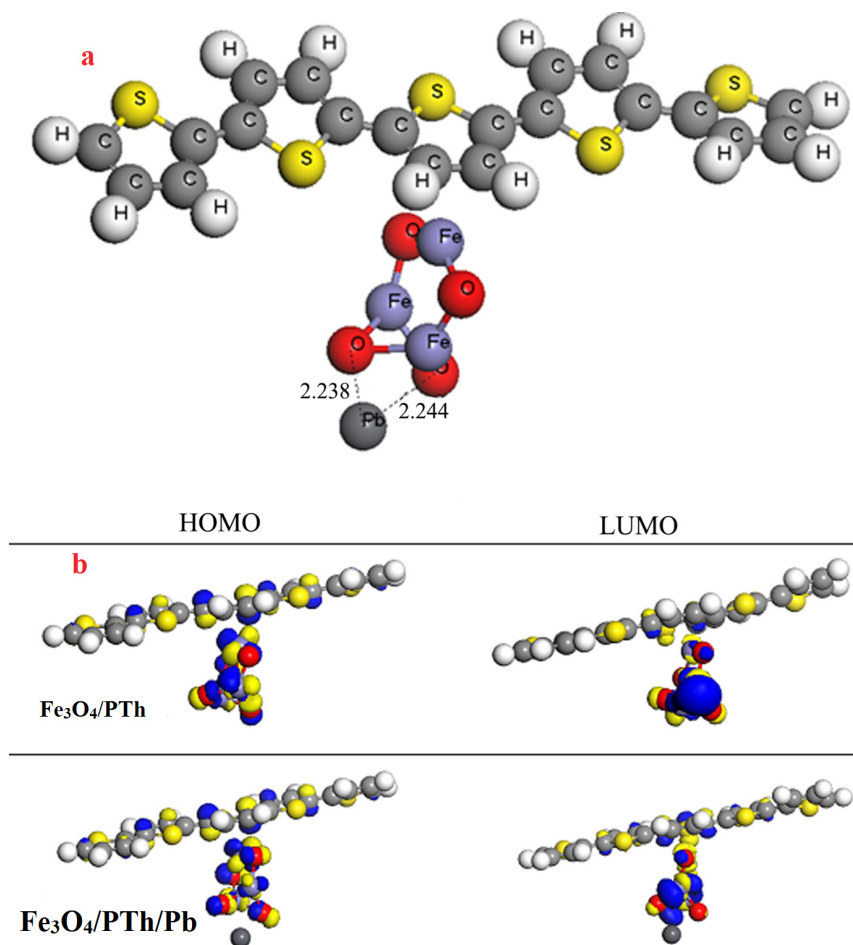


Fig. 10. (a) The most stable adsorption configuration of Pb on the surface of  $\text{Fe}_3\text{O}_4/\text{PTh}$  nanocomposite and b) the spatial distribution of HOMO and LUMO of the  $\text{Fe}_3\text{O}_4/\text{PTh}$  and the structure of Pb-adsorbed form of  $\text{Fe}_3\text{O}_4/\text{PTh}$  nanocomposite. (Distances are in Å).

face, small changes are found in the distribution of frontier molecular orbitals, which shows that the Pb adsorption has a low effect on the electronic structure of the nanocomposite.

The observed results suggest that this interaction is between the physisorption, with negligible perturbation on the electronic structure upon adsorption process, and chemisorption, with significant adsorption energy. Therefore, despite the relatively high adsorption energy of Pb, the  $\text{Fe}_3\text{O}_4/\text{PTh}$  nanocomposite can be reused for lead ion adsorption.

#### 4. Conclusions

In the current study, a batch adsorption experiment was conducted with the aim to remove Pb(II) from aqueous solutions by  $\text{Fe}_3\text{O}_4/\text{PTh}$  adsorbent. Obtained adsorption efficiency and capacity for removal of Pb(II) from aqueous solution were acceptable. The results showed that the performance of adsorbent is strongly dependent on the pH and temperature of the solution and 100% removal was obtained at pH 6 and 60°C, respectively when the adsorbent dose was 10 g/L. Adsorption equilibrium was gained after

60 min. Investigating adsorption kinetics demonstrated linear pseudo-second-order has the best description to model the adsorption of Pb(II). Linear Sips adsorption isotherm model was the best model to fit Pb(II) equilibrium adsorption data. The maximum obtained adsorption capacity ( $q_{max}$ ) was 47.577 mg/g. DFT study results reveal that Pb(II) prefer to be adsorbed near the  $\text{Fe}_3\text{O}_4$  site of the  $\text{Fe}_3\text{O}_4/\text{PTh}$  nanocomposite with the adsorption energy of  $-272.11$  kJ/mol. The positive values of  $\Delta H^\circ$  and negative of  $\Delta G^\circ$  imply the endothermic nature and spontaneous of the adsorption process, respectively. According to the desorption studies,  $\text{Fe}_3\text{O}_4/\text{PTh}$  nanocomposite could be used again for five successive adsorption-desorption cycles without any noticeable decline in removal efficiency.

#### Symbols

$a_R$ (1/mg) <sup>BR</sup>	— Redlich–Peterson isotherm constant
$a_s$ (L/mg)	— Sips isotherm model constant
$A_T$ (L/g)	— Tempkin isotherm equilibrium binding constant
$b$ (J/mol)	— Tempkin isotherm heat of sorption constant

$b_R$	— Redlich-Peterson isotherm exponent
$C_0$ (mg/L)	— Adsorbate initial concentration
$C_e$ (mg/L)	— Adsorbate equilibrium concentration
$C_t$ (mg/L)	— Adsorbate concentration at the time t
$C_i$ (mg/L)	— Highest adsorbate initial concentration
$E_{ad}$ (eV) or (kJ/mol)	— Adsorption energy
$E_{tot}$ (eV) or (kJ/mol)	— Total energy of the adsorption structure
$\Delta G^0$ (kJ/mol.K)	— Gibbs free energy
$\Delta H^0$ (kJ/mol)	— Enthalpy
$K$	— Adsorption distribution coefficient
$K_f$ (mg/g)(dm <sup>3</sup> /g) $\eta$	— Freundlich isotherm constant related to adsorption capacity
$K_1$ (1/min)	— Pseudo-first-order rate constant
$K_2$ (g/mg·min)	— Pseudo-second-order rate constant
$K_L$ (L/mg)	— Langmuir isotherm constant
$K_R$ (L/g)	— Redlich-Peterson isotherm constant
$n_s$ (-)	— Sips isotherm exponent
$Q_{max}$ (mg/g)	— Maximum adsorption capacity
$q_e$ (mg/g)	— Amount of adsorbate in the adsorbent at equilibrium
$q_m$ (mg/g)	— Maximum amount of monolayer adsorption
$q_t$ (mg/g)	— Amount of adsorbate in the adsorbent at the time t
$R$ (J/mol.K)	— Universal gas constant
$R_L$ (-)	— Separation factor
$\Delta S^0$ (kJ/mol)	— Entropy
$T$ (K)	— Temperature
$\eta$ (-)	— Adsorption intensity

## References

- [1] A.A. Farghali, M. Bahgat, A. Enaiet Allah, M.H. Khedr, Adsorption of Pb(II) ions from aqueous solutions using copper oxide nanostructures, Beni-Suef Uni. J. Basic Appl. Sci., 2 (2013) 61–71.
- [2] Y. Huang, S. Li, J. Chen, X. Zhang, Y. Chen, Adsorption of Pb (II) on mesoporous activated carbons fabricated from water hyacinth using H<sub>3</sub>PO<sub>4</sub> activation: adsorption capacity, kinetic and isotherm studies, Appl. Surf. Sci., 293 (2014) 160–168.
- [3] J.M. Dias, M.C.M. Alvim-Ferraz, M.F. Almeida, J. Rivera-Utrilla, M. Sánchez-Polo, Waste materials for activated carbon preparation and its use in aqueous-phase treatment: A review, J. Environ. Manage., 85 (2007) 833–846.
- [4] M. Bhaumik, A. Maity, V.V. Srinivasu, M.S. Onyango, Enhanced removal of Cr(VI) from aqueous solution using polypyrrole/Fe<sub>3</sub>O<sub>4</sub> magnetic nanocomposite, J. Hazard. Mater., 190 (2011) 381–390.
- [5] J. Salimi, B. Kakavandi, A.A. Babaei, A. Takdastan, N. Alavi, A. Neisi, B. Ayoubi-Feiz, Modeling and optimization of nonylphenol removal from contaminated water media using a magnetic recoverable composite by artificial neural networks, Water Sci. Technol., 75 (2017) 1761–1775.
- [6] A.A. Babaei, B. Kakavandi, M. Rafiee, F. Kalantarhormizi, I. Purkaram, E. Ahmadi, S. Esmaili, Comparative treatment of textile wastewater by adsorption, Fenton, UV-Fenton and US-Fenton using magnetic nanoparticles-functionalized carbon (MNP@C), J. Ind. Eng. Chem., 56 (2017) 163–174.
- [7] E.-J. Woo, H.-S. Kwon, C.-H. Lee, Preparation of nano-magnetite impregnated mesocellular foam composite with a Cu ligand for His-tagged enzyme immobilization, Chem. Eng. J., 274 (2015) 1–8.
- [8] Z.M. Saiyed, M. Parasramka, S.D. Telang, C.N. Ramchand, Extraction of DNA from agarose gel using magnetic nanoparticles (magnetite or Fe<sub>3</sub>O<sub>4</sub>), Anal. Biochem., 363 (2007) 288–290.
- [9] J.-M. Shen, F.-Y. Gao, T. Yin, H.-X. Zhang, M. Ma, Y.-J. Yang, F. Yue, cRGD-functionalized polymeric magnetic nanoparticles as a dual-drug delivery system for safe targeted cancer therapy, Pharmacol. Res., 70 (2013) 102–115.
- [10] C.-C. Liu, S. Sadhasivam, S. Savitha, F.-H. Lin, Fabrication of multiwalled carbon nanotubes-magnetite nanocomposite as an effective ultra-sensing platform for the early screening of nasopharyngeal carcinoma by luminescence immunoassay, Talanta, 122 (2014) 195–200.
- [11] M. Usman, P. Faure, K. Hanna, M. Abdelmoula, C. Ruby, Application of magnetite catalyzed chemical oxidation (Fenton-like and persulfate) for the remediation of oil hydrocarbon contamination, Fuel, 96 (2012) 270–276.
- [12] M. Munoz, Z.M. de Pedro, J.A. Casas, J.J. Rodriguez, Preparation of magnetite-based catalysts and their application in heterogeneous Fenton oxidation – A review, Appl. Catal., B: Environ., 176–177 (2015) 249–265.
- [13] E. Ranjith Kumar, R. Jayaprakash, G. Sarala Devi, P. Siva Prasada Reddy, Synthesis of Mn substituted CuFe<sub>2</sub>O<sub>4</sub> nanoparticles for liquefied petroleum gas sensor applications, Sens. Actuators, B: Chem., 191 (2014) 186–191.
- [14] D. Ramimoghdam, S. Bagheri, S.B.A. Hamid, Progress in electrochemical synthesis of magnetic iron oxide nanoparticles, J. Magn. Magn. Mater., 368 (2014) 207–229.
- [15] X.S. Wang, L. Zhu, H.J. Lu, Surface chemical properties and adsorption of Cu (II) on nanoscale magnetite in aqueous solutions, Desalination, 276 (2011) 154–160.
- [16] L. Rahmanzadeh, M. Ghorbani, M. Jahanshahi, Synthesis and Characterization of Fe<sub>3</sub>O<sub>4</sub> @ Polyrhodanine Nanocomposite with Core-Shell Morphology, Adv. Polym. Tech., 33 (2014) 1–5.
- [17] E. Karaca, M. Şatır, S. Kazan, M. Açıkgöz, E. Öztürk, G. Gürdağ, D. Ulutaş, Synthesis, characterization and magnetic properties of Fe<sub>3</sub>O<sub>4</sub> doped chitosan polymer, J. Magn. Magn. Mater., 373 (2015) 53–59.
- [18] D. Aradilla, F. Estrany, F. Casellas, J.I. Iribarren, C. Alemán, All-polythiophene rechargeable batteries, Org. Electron., 15 (2014) 40–46.
- [19] T. Vu Quoc, T. Duong Ngoc, H. Duong Ngoc, Polypyrrole/Al<sub>2</sub>O<sub>3</sub> nanocomposites: preparation, characterisation and electromagnetic shielding properties, J. Exp. Nanosci., 4 (2009) 213–219.
- [20] H. Qin, A. Kulkarni, H. Zhang, H. Kim, D. Jiang, T. Kim, Polypyrrole thin film fiber optic chemical sensor for detection of VOCs, Sens. Actuators, B: Chem., 158 (2011) 223–228.
- [21] L. Sicot, C. Fiorini, A. Lorin, P. Raimond, C. Sentein, J.-M. Nunzi, Improvement of the photovoltaic properties of polythiophene-based cells, Sol. Energy Mater. Sol. Cells, 63 (2000) 49–60.
- [22] Y. Gupta, K. Hellgardt, R.J. Wakeman, Enhanced permeability of polyaniline based nano-membranes for gas separation, J. Membr. Sci., 282 (2006) 60–70.
- [23] Q. Xu, J.-J. Zhu, X.-Y. Hu, Ordered mesoporous polyaniline film as a new matrix for enzyme immobilization and biosensor construction, Anal. Chim. Acta, 597 (2007) 151–156.
- [24] F.X. Perrin, T.A. Phan, D.L. Nguyen, Preparation and characterization of polyaniline in reversed micelles of decylphosphonic acid for active corrosion protection coatings, Eur. Polym. J., 66 (2015) 253–265.
- [25] M. Ghorbani, H. Esfandian, N. Taghipour, R. Katal, Application of polyaniline and polypyrrole composites for paper mill wastewater treatment, Desalination, 263 (2010) 279–284.
- [26] S.W. Phang, M. Tadokoro, J. Watanabe, N. Kuramoto, Microwave absorption behaviors of polyaniline nanocomposites containing TiO<sub>2</sub> nanoparticles, Curr. Appl. Phys., 8 (2008) 391–394.
- [27] F. Entezari Juybari, A. Kamran-Pirzaman, M. Ghorbani, Chemical modification of magnetite with polythiophene and

- characterization of formed core-shell nanocomposite, *Inorg. Nano-Met. Chem.*, 47 (2017) 121–126.
- [28] B. Delley, From molecules to solids with the DMol3 approach, *J. Chem. Phys.*, 113 (2000) 7756–7764.
- [29] J.P. Perdew, K. Burke, M. Ernzerhof, Generalized gradient approximation made simple, *Phys. Rev. Lett.*, 77 (1996) 3865–3868.
- [30] B. Delley, A scattering theoretic approach to scalar relativistic corrections on bonding, *Int. J. Quantum Chem.*, 69 (1998) 423–433.
- [31] D. Farmanzadeh, L. Tabari, DFT study of adsorption of picric acid molecule on the surface of single-walled ZnO nanotube; as potential new chemical sensor, *Appl. Surf. Sci.*, 324 (2015) 864–870.
- [32] J. Casado, V. Hernández, S. Hotta, J.T. López Navarrete, Vibrational spectra of charged defects in a series of  $\alpha$ ,  $\alpha'$ -dimethyl end-capped oligothiophenes induced by chemical doping with iodine, *J. Chem. Phys.*, 109 (1998) 10419–10429.
- [33] T.P. Kaloni, G. Schreckenbach, M.S. Freund, Structural and electronic properties of pristine and doped polythiophene: periodic versus molecular calculations, *J. Chem. Phys. C*, 119 (2015) 3979–3989.
- [34] S.R. Chowdhury, E.K. Yanful, Arsenic and chromium removal by mixed magnetite–maghemite nanoparticles and the effect of phosphate on removal, *J. Environ. Manage.*, 91 (2010) 2238–2247.
- [35] F. Zhao, W.Z. Tang, D. Zhao, Y. Meng, D. Yin, M. Sillanpää, Adsorption kinetics, isotherms and mechanisms of Cd(II), Pb(II), Co(II) and Ni(II) by a modified magnetic polyacrylamide microcomposite adsorbent, *J. Water Process. Eng.*, 4 (2014) 47–57.
- [36] N.N. Nassar, Rapid removal and recovery of Pb (II) from wastewater by magnetic nano-adsorbents, *J. Hazard. Mater.*, 184 (2010) 538–546.
- [37] Y.S. Ho, G. McKay, Pseudo-second order model for sorption processes, *Process. Biochem.*, 34 (1999) 451–465.
- [38] M. Ahmadi, H. Rahmani, B. Ramavandi, B. Kakavandi, Removal of nitrate from aqueous solution using activated carbon modified with Fenton reagents, *Desal. Water Treat.*, 76 (2017) 265–275.
- [39] K.Y. Foo, B.H. Hameed, Insights into the modeling of adsorption isotherm systems, *Chem. Eng. J.*, 156 (2010) 2–10.
- [40] Y.S. Ho, J.F. Porter, G. McKay, Equilibrium isotherm studies for the sorption of divalent metal ions onto peat: copper, nickel and lead single component systems, *Water, Air, Soil Pollut.*, 141 (2002) 1–33.
- [41] H. Shahbeig, N. Bagheri, S.A. Ghorbanian, A. Hallajisani, S. Poorkarimi, A new adsorption isotherm model of aqueous solutions on granular activated carbon, *World J. Modell. Simul.*, 9 (2013) 243–254.
- [42] N. Kumara, N. Hamdan, M.I. Petra, K.U. Tennakoon, P. Ekanayake, Equilibrium isotherm studies of adsorption of pigments extracted from kuduk-kuduk (*Melastoma malabathricum* L.) pulp onto TiO<sub>2</sub> nanoparticles, *J. Chem.*, 2014 (2014).
- [43] M. Kumari, C.U. Pittman Jr, D. Mohan, Heavy metals [chromium (VI) and lead (II)] removal from water using mesoporous magnetite (Fe<sub>3</sub>O<sub>4</sub>) nanospheres, *J. Colloid Interface Sci.*, 442 (2015) 120–132.
- [44] H. Yousefzadeh, A.A. Salarian, H. Sid Kalal, Study of Pb (II) adsorption from aqueous solutions by TiO<sub>2</sub> functionalized with hydroxide ethyl aniline (PHEA/n-TiO<sub>2</sub>), *J. Mol. Liq.*, 263 (2018) 294–302.
- [45] A.Z.M. Badruddoza, Z.B.Z. Shawon, W.J.D. Tay, K. Hidajat, M.S. Uddin, Fe<sub>3</sub>O<sub>4</sub>/cyclodextrin polymer nanocomposites for selective heavy metals removal from industrial wastewater, *Carbohydr. Polym.*, 91 (2013) 322–332.
- [46] M. Mozaffari, M.R.S. Emami, E. Binaeian, A novel thiosemicarbazide modified chitosan (TSFCS) for efficiency removal of Pb (II) and methyl red from aqueous solution, *Int. J. Biol. Macromol.* (2018).
- [47] C.M. Futralan, C.-C. Kan, M.L. Dalida, K.-J. Hsien, C. Pascua, M.-W. Wan, Comparative and competitive adsorption of copper, lead, and nickel using chitosan immobilized on bentonite, *Carbohydr. Polym.*, 83 (2011) 528–536.
- [48] S. Cataldo, A. Gianguzza, D. Milea, N. Muratore, A. Pettignano, Pb(II) adsorption by a novel activated carbon - alginate composite material. A kinetic and equilibrium study, *Int. J. Biol. Macromol.*, 92 (2016) 769–778.
- [49] A. Idris, N.S.M. Ismail, N. Hassan, E. Misran, A.-F. Ngomsik, Synthesis of magnetic alginate beads based on maghemite nanoparticles for Pb(II) removal in aqueous solution, *J. Ind. Eng. Chem.*, 18 (2012) 1582–1589.
- [50] B. Kakavandi, A. Jonidi Jafari, R. Rezaei Kalantary, S. Nasser, A. Esrafil, A. Gholizadeh, A. Azari, Simultaneous adsorption of lead and aniline onto magnetically recoverable carbon: Optimization, modeling and mechanism, *J. Chem. Technol. Biotechnol.*, 91 (2016) 3000–3010.
- [51] M. Ghorbani, H. Eisazadeh, Removal of COD, color, anions and heavy metals from cotton textile wastewater by using polyaniline and polypyrrole nanocomposites coated on rice husk ash, *Composites Part B: Eng.*, 45 (2013) 1–7.
- [52] P.K. Boruah, D.J. Borah, J. Handique, P. Sharma, P. Sengupta, M.R. Das, Facile synthesis and characterization of Fe<sub>3</sub>O<sub>4</sub> nanopowder and Fe<sub>3</sub>O<sub>4</sub>/reduced graphene oxide nanocomposite for methyl blue adsorption: A comparative study, *J. Environ. Chem. Eng.*, 3 (2015) 1974–1985.
- [53] X. He, R. Che, Y. Wang, Y. Li, L. Wan, X. Xiang, Core–nanoshell magnetic composite material for adsorption of Pb(II) in wastewater, *J. Environ. Chem. Eng.*, 3 (2015) 1720–1724.
- [54] É.G. Bajnóczi, I. Pálincó, T. Körtvélyesi, S. Bálint, I. Bakó, P. Sipos, I. Persson, Speciation and the structure of lead(II) in hyper-alkaline aqueous solution, *Dalton Trans.*, 43 (2014) 17539–17543.